

Parametric Quantum State Tomography with HyperRBMs

Simon Tonner^{1a}, Viet T. Tran^{1ab} and Richard Kueng¹

¹*Department for Quantum Information and Computation at Kepler (QUICK), Johannes Kepler University, Linz, Austria*

Keywords: Quantum State Tomography, Machine Learning, Restricted Boltzmann Machines, Hypernetworks, Parametric Learning, Ising Model.

Abstract: Quantum state tomography (QST) is essential for validating quantum devices but suffers from exponential scaling in system size. Neural-network quantum states, such as Restricted Boltzmann Machines (RBMs), can efficiently parameterize individual many-body quantum states and have been successfully used for QST. However, existing approaches are point-wise and require retraining at every parameter value in a phase diagram. We introduce a parametric QST framework based on a hypernetwork that conditions an RBM on Hamiltonian control parameters, enabling a single model to represent an entire family of quantum ground states. Applied to the transverse-field Ising model, our HyperRBM achieves high-fidelity reconstructions from local Pauli measurements on 1D and 2D lattices across both phases and through the critical region. Crucially, the model accurately reproduces the fidelity susceptibility and identifies the quantum phase transition without prior knowledge of the critical point. These results demonstrate that hypernetwork-modulated neural quantum states provide an efficient and scalable route to tomographic reconstruction across full phase diagrams.

1 INTRODUCTION

Extracting complete information about an unknown quantum state from measurement data requires the full reconstruction of a classical description of its wavefunction or density matrix. This process, known as quantum state tomography (QST) [1, 2, 3], is a fundamental tool across quantum science, enabling validation and benchmarking of quantum devices. The computational cost of QST typically scales exponentially with system size, although polynomially scaling algorithms exist for certain restricted classes of states [4, 5]. However, the sample requirements of general QST also scale exponentially. This holds even for the most sample-efficient tomographic protocols currently known [6, 7, 8, 9, 10] and reflects a fundamental limitation of general-purpose QST.

Shifting the goal from full state reconstruction to estimating specific properties allows for polylogarithmic sample complexity. While highly efficient, this approach of *shadow tomography* [11, 12, 13] does not provide a full tomographic description of the quantum state. Relatedly, a recent line of work studies how to predict ground-state properties of local, gapped Hamiltonians by learning from data drawn from other Hamiltonians in the same phase. These approaches leverage locality and

classical-shadow style representations to obtain provable sample-complexity guarantees for estimating target observables within a phase, improving from polynomial to logarithmic and even constant sample complexity under additional assumptions [14, 15, 16]. Despite these rigorous guarantees for learning specific observables, these methods do not aim to reconstruct a full state representation across the phase diagram.

To achieve full state reconstruction with reduced complexity, alternative strategies incorporate physical assumptions. Methods such as matrix product state (MPS) tomography [17, 18] and compressed sensing [8, 19] exploit low entanglement or low rank but are limited to specific classes of states. More recently, machine learning (ML) techniques have emerged as powerful tools to address the curse of dimensionality in many-body quantum systems [20]. RBMs specifically have proven to be efficient ansatzes for QST capable of reconstructing highly entangled states [21, 22]. In these neural-network quantum states (NQS) representations, the wavefunction is compactly encoded in a network of stochastic neurons [20]. Despite their success, existing neural QST methods do not readily accommodate the study of phase diagrams, which are mapped out by varying a Hamiltonian control parameter. In practice, this requires training a separate model for each parameter value, resulting in significant computational and data inefficiencies.

^aThese authors contributed equally.

^bCorresponding author: viet_thuong.tran@jku.at

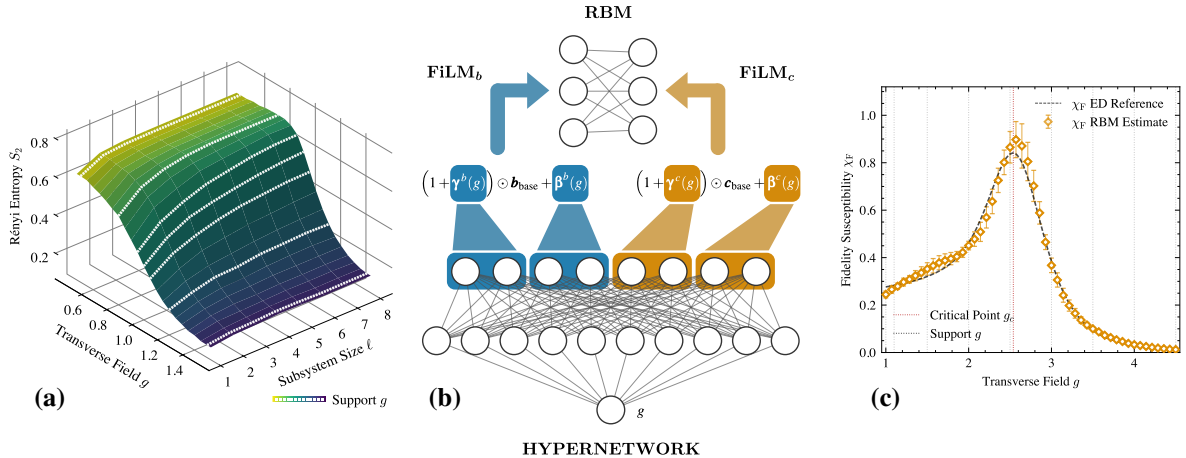


Figure 1: **HyperRBM reconstruction of Rényi entropy and susceptibility in the transverse-field Ising model (TFIM).** (a) Second Rényi entropy $S_2(g)$ for the ground state of the 4×4 transverse-field Ising model for various subsystem sizes and transverse field strengths g . All results are obtained from a single HyperRBM trained on local Pauli measurements. Solid lines indicate exact values from exact diagonalization. (b) HyperRBM architecture. A hypernetwork acts as conditioner and takes the control parameter g and outputs feature-wise linear modulation coefficients γ and β , which affinely modulate the restricted Boltzmann machine (RBM) biases in visible and hidden layers. (c) Fidelity susceptibility $\chi_F(g)$ of the 4×4 TFIM. Orange markers show HyperRBM estimates from free-energy gradient variance (Sec. 4.2.2), gray dashed curves indicate ED references. Vertical gray dotted lines mark support field strengths, and the red dotted line indicates the finite-size critical field g_c . The reconstructed $\chi_F(g)$ reproduces the ED peak in the crossover region.

cies. In this sense, current neural QST approaches are inherently *point-wise*, treating each parameter value as an independent learning problem and ignoring correlations between nearby states in parameter space.

Several approaches partially address this limitation. In one recent approach, parametric quantum state tomography (pQST) is formulated as a classical post-processing problem, where the parameter dependence of the quantum state is assumed to admit an expansion in a fixed function basis [23]. Standard point-wise tomography is performed at randomly sampled parameter values, and the resulting estimates are combined using compressed-sensing techniques to reconstruct the full parameterized family. In this approach, the parametric structure is fixed *a priori*, and learning occurs only at the level of the expansion coefficients, rather than through a learned parametric state representation.

From a complementary perspective, conditional generative models have also been applied to quantum state tomography. Conditional generative adversarial networks [24], for example, have been used to learn a direct map from measurement data to a physical density matrix, enabling fast reconstruction across related experiments. While these methods introduce conditioning at the level of the generative model, they remain intrinsically point-wise: each reconstructed state is tied to a specific dataset and does not encode smooth parametric dependence on an underlying

Hamiltonian. As a result, they do not provide access to quantities that rely on the continuity and differentiability of the state manifold, such as fidelity susceptibility.

A natural way to overcome these limitations is to learn the parametric dependence directly at the level of the quantum state ansatz itself. Hypernetworks [25, 26, 27], which generate or modulate the parameters of another network as a function of external inputs, provide a principled mechanism for this purpose and have found success in meta-learning and conditional generative modeling [26, 28, 29]. When applied to neural-network quantum states, this construction yields a differentiable family of wavefunctions conditioned on Hamiltonian parameters, enabling state reconstruction across an entire phase diagram. Crucially, treating the reconstructed states as a coherent parametric family allows us to extract the fidelity susceptibility directly from the learned model and to identify quantum phase transitions without prior knowledge of the critical point.

This motivates our work. We introduce a pQST framework based on a hypernetwork-modulated NQS that learns an entire family of ground states across a phase diagram within a single model. We build on the RBM-based tomography of [21] by employing a lightweight hypernetwork implemented via feature-wise linear modulation (FiLM) [30] to condition the RBM biases on an external Hamiltonian parameter.

We apply this HyperRBM architecture on the 1D and 2D TFIM and demonstrate high fidelity reconstructions of ground states across both ferromagnetic and paramagnetic phases, including the critical region. Specifically, we consider a one-dimensional chain of size 16 and two-dimensional square lattices of size $L \times L$ with $L \in \{3, 4\}$. Moreover, we show for the first time that an RBM-based approach can predict the fidelity susceptibility, enabling the identification of the quantum phase transition without prior knowledge of the critical point [31, 32]. This demonstrates that pQST captures not only the wavefunctions, but also higher-order parametric responses typically challenging for generative models.

While ML approaches have been widely used for phase classification [33, 34, 35], they focus on identifying phase boundaries rather than reconstructing quantum states. In contrast, our goal is a conditional generative model that captures the full parametric dependence of the state, enabling the evaluation of physical observables throughout the phase diagram.

The paper is organized as follows. Section 2 introduces the physical setting and reviews RBMs as neural-network quantum states. Section 3 presents our HyperRBM architecture for parametric QST. Section 4 defines our evaluation metrics, covering both local observables and global state-level diagnostics. Section 5 describes data generation and training details. Section 6 reports the main reconstruction results across the phase diagram. We conclude with a summary and outlook in Section 7.

2 THEORY

2.1 Neural-network quantum states and parametric tomography

A central challenge in quantum many-body physics is the exponential growth of Hilbert space dimension. A generic wavefunction of N spins,

$$|\Psi\rangle = \sum_s \Psi(s) |s\rangle, \quad (1)$$

requires 2^N complex-valued coefficients in a fixed product basis $\{|s\rangle\}$ with $s \in \{0, 1\}^N$. Neural-network quantum states (NQS) address this issue by replacing the explicit storage of amplitudes with a parameterized function that approximates the mapping $s \mapsto \Psi(s) \in \mathbb{C}$.

In quantum state tomography, the wavefunction is not given explicitly but accessed through quantum measurement data. We consider a *parametric* tomography setting in which the quantum state depends on

an external control parameter g . This parameter may represent a Hamiltonian control variable (e.g., transverse field strength). The goal is to learn a single conditional model $p_\theta(\cdot | g)$ that captures a continuous family of quantum states from measurement data collected at multiple parameter values.

For general quantum states, reconstructing $\Psi(s)$ requires learning both amplitudes and phases and typically necessitates measurements in multiple bases. In this work, we focus on ground states of *stoquastic* Hamiltonians. As a consequence of the Perron-Frobenius theorem, these states can be chosen to be real-valued and non-negative in the fixed product basis, i.e. $\Psi(s | g) \geq 0$ for all s [36]. In this setting, the quantum state is fully characterized by the probability distribution of measurement outcomes in the computational (σ^z) basis,

$$q(s | g) = |\Psi(s | g)|^2, \quad (2)$$

and quantum state reconstruction reduces to learning this distribution from data. The training dataset consists of tuples $(s^{(i)}, g^{(i)})$ collected at multiple values of g . In the following we realize the conditional model $p_\theta(s | g)$ with a RBM.

2.2 Restricted Boltzmann machines

For completeness and to make the later conditioning mechanism explicit, we begin by briefly reviewing the standard RBM formulation for modeling a single quantum state and highlight the parameters (biases) that will be modulated by the FiLM hypernetwork in Sec. 3, before extending it to a conditional, parameter-dependent model in Sec. 3.2.

To represent probability distributions over high-dimensional binary variables, we employ a RBM [37, 38] which is a bipartite energy-based model defined on a set of binary visible units $\mathbf{v} = (v_1, \dots, v_N)$ and binary hidden units $\mathbf{h} = (h_1, \dots, h_M)$. The joint distribution is given by the Boltzmann form

$$p_\theta(\mathbf{v}, \mathbf{h}) = \frac{1}{Z_\theta} \exp[-E_\theta(\mathbf{v}, \mathbf{h})], \quad (3)$$

with energy function

$$E_\theta(\mathbf{v}, \mathbf{h}) = -\sum_i b_i v_i - \sum_j c_j h_j - \sum_{i,j} v_i W_{ij} h_j, \quad (4)$$

where $\theta = \{\mathbf{W}, \mathbf{b}, \mathbf{c}\}$ denotes the set of trainable parameters and $Z_\theta = \sum_{\mathbf{v}, \mathbf{h}} e^{-E_\theta(\mathbf{v}, \mathbf{h})}$ is the partition function. The bias terms \mathbf{b} and \mathbf{c} enter additively in the energy and will be the quantities modified in our parametric extension (see Sec. 3.3).

Marginalizing over the hidden variables \mathbf{h} yields the model distribution over visible configurations

$$p_\theta(\mathbf{v}) = \frac{1}{Z_\theta} \sum_{\mathbf{h}} e^{-E_\theta(\mathbf{v}, \mathbf{h})} = \frac{1}{Z_\theta} e^{-F_\theta(\mathbf{v})}. \quad (5)$$

Here, $F_\theta(\mathbf{v})$ is the free energy given by

$$F_\theta(\mathbf{v}) = -\sum_i b_i v_i - \sum_j \text{softplus}((\mathbf{W}^\top \mathbf{v})_j + c_j), \quad (6)$$

where $\text{softplus}(x) = \log(1 + e^x)$ arises from analytically summing over all binary hidden units.

The bipartite structure implies conditional independence between visible and hidden variables, allowing efficient block Gibbs sampling and tractable evaluation of $F_\theta(\mathbf{v})$, which is the central quantity entering training, sampling, and observable estimation.

2.3 Training and contrastive divergence

RBM training is formulated as the minimization of the Kullback–Leibler (KL) divergence between the empirical data distribution $q(\mathbf{v})$ and the model distribution $p_\theta(\mathbf{v})$:

$$D_{\text{KL}}(q \parallel p_\theta) = \sum_{\mathbf{v}} q(\mathbf{v}) \log \frac{q(\mathbf{v})}{p_\theta(\mathbf{v})}. \quad (7)$$

Taking the gradient with respect to θ and noting that the entropy of q is independent of the model parameters, one finds

$$\nabla_\theta D_{\text{KL}} = -\sum_{\mathbf{v}} q(\mathbf{v}) \nabla_\theta \log p_\theta(\mathbf{v}). \quad (8)$$

Using $\log p_\theta(\mathbf{v}) = -F_\theta(\mathbf{v}) - \log Z_\theta$, the gradient of the log partition function can be expressed as an expectation value:

$$\begin{aligned} \nabla_\theta \log Z_\theta &= \frac{1}{Z_\theta} \sum_{\mathbf{v}} e^{-F_\theta(\mathbf{v})} (-\nabla_\theta F_\theta(\mathbf{v})) \\ &= -\mathbb{E}_{p_\theta} [\nabla_\theta F_\theta(\mathbf{v})]. \end{aligned} \quad (9)$$

Substituting this back yields the gradient of the KL divergence as:

$$\nabla_\theta D_{\text{KL}} = \mathbb{E}_q [\nabla_\theta F_\theta(\mathbf{v})] - \mathbb{E}_{p_\theta} [\nabla_\theta F_\theta(\mathbf{v})]. \quad (10)$$

The first term, known as the positive phase, lowers the free energy of configurations observed in the data. The second term, the negative phase, raises the free energy of configurations sampled from the model. While the positive phase is evaluated directly on data samples, the negative phase requires sampling from $p_\theta(\mathbf{v})$. Exact sampling is intractable for large systems; therefore, the expectation \mathbb{E}_{p_θ} is approximated using contrastive divergence (CD- k) [37]. In this scheme, short Gibbs chains are initialized at data configurations to obtain samples \mathbf{v}_{CD} .

Finally, the model parameters are updated using stochastic gradient descent. Based on the approximated gradient from Eq. (10), the update rule is given by:

$$\theta^{(t+1)} \leftarrow \theta^{(t)} - \eta \left(\mathbb{E}_q [\nabla_\theta F_\theta(\mathbf{v})] - \mathbb{E}_{p_{CD}} [\nabla_\theta F_\theta(\mathbf{v}_{CD})] \right), \quad (11)$$

where η is the learning rate.

2.4 Application to Ising-type ground states

We now connect the RBM formalism to quantum spin systems. For the transverse-field Ising model, the visible units are identified with spin configurations in the computational basis. To align with the physical spin values, we formulate the RBM visible units as $\mathbf{v} \equiv \mathbf{s} \in \{0, 1\}^N$.

Since the ground states considered here are known to be real-valued and non-negative (due to the stoquasticity of the Hamiltonian), the trained RBM parametrizes the wavefunction amplitude directly:

$$\Psi_\theta(\mathbf{s}) = \sqrt{p_\theta(\mathbf{s})}. \quad (12)$$

While we restrict our attention here to stoquastic Hamiltonians to isolate the problem of learning the parametric dependence on g , the hypernetwork formalism can be extended to complex-valued states by using two (Hyper)RBMs to parametrize the amplitude and phase separately, as demonstrated in Ref. [21].

3 METHODS

3.1 Problem setup: Transverse-field Ising model

We study ground states of TFIM in one and two spatial dimensions. The Hamiltonian is given by

$$H(g) = -J \sum_{\langle i, j \rangle} \sigma_i^z \sigma_j^z - g \sum_{i=1}^N \sigma_i^x, \quad (13)$$

where, $J > 0$ is the ferromagnetic coupling and g is the transverse-field strength, serving as our continuous control parameter.

We consider two distinct geometries with periodic boundary conditions:

- (i) **1D Chain:** A single one-dimensional chain consisting of $N = 16$ spins.
- (ii) **2D Lattices:** Two-dimensional square lattices of size $L \times L$ with $L \in \{3, 4\}$ corresponding to $N = 9$ and $N = 16$ spins, respectively.

For a set of support points $\{g_i\}$, we collect measurement samples $\{(\mathbf{s}^{(j)}, g^{(j)})\}$ in the computational basis. The goal is to train a single conditional model $p_\theta(\mathbf{s} \mid g)$ that accurately interpolates across the entire range of g for each geometry. Reference ground states $|\Psi_{\text{ED}}(g)\rangle$ are computed via Lanczos exact diagonalization (ED) for benchmarking.

3.2 Conditional RBM energy

We model the conditional distribution $p_\theta(\mathbf{s} | g)$ using an RBM as introduced in Sec. 2. The visible units $\mathbf{s} \in \{0,1\}^N$ represent measurement outcomes in the computational basis, while the hidden units $\mathbf{h} \in \{0,1\}^M$ encode correlations between spins. The interaction weights $\mathbf{W} \in \mathbb{R}^{N \times M}$ are shared across all values of g , while the bias parameters are functions of the control parameter.

Conditioned on g , the RBM energy is (compare Eq. (4)):

$$E_\theta(\mathbf{s}, \mathbf{h} | g) = -\sum_i b_i(g) s_i - \sum_j c_j(g) h_j - \sum_{i,j} s_i W_{ij} h_j, \quad (14)$$

The corresponding free energy $F_\theta(\mathbf{s} | g)$ and model distribution $p_\theta(\mathbf{s} | g)$ are defined analogously to Eqs. (5) and (6). Exploiting stoquasticity and following Eq. (12), we define the conditional wavefunction as

$$\Psi_\theta(\mathbf{s} | g) := \sqrt{p_\theta(\mathbf{s} | g)}. \quad (15)$$

3.3 Hypernetwork-based conditioning

This construction is conceptually related to conditional RBMs [39], where external variables enter the model through linear modulations of the bias terms. We generalize this idea by using a hypernetwork to implement a nonlinear modulation of the RBM biases as a function of the control parameter g . Specifically, a lightweight multilayer perceptron (MLP) takes g as input and outputs feature-wise scale and shift parameters for the visible and hidden biases.

Using FiLM [30], the biases are modulated as

$$\mathbf{b}(g) = \left(1 + \boldsymbol{\gamma}^b(g)\right) \odot \mathbf{b}_{\text{base}} + \boldsymbol{\beta}^b(g), \quad (16)$$

$$\mathbf{c}(g) = \left(1 + \boldsymbol{\gamma}^c(g)\right) \odot \mathbf{c}_{\text{base}} + \boldsymbol{\beta}^c(g), \quad (17)$$

where \odot denotes the Hadamard product. This results in the architecture shown in Fig. 1(b).

3.4 Symmetrized free energy

In the ferromagnetic phase of the TFIM ($g < J$), the ground state is doubly degenerate, corresponding to all spins aligning up or down. A standard RBM often breaks this symmetry spontaneously, converging to only one of the two attractors. To strictly enforce the physical \mathbb{Z}_2 spin-flip symmetry, we adopt a symmetrized ansatz where the probability is modeled as an equal superposition of a configuration \mathbf{s} and its in-

verse $1 - \mathbf{s}$:

$$p_{\text{sym}}(\mathbf{s} | g) \propto e^{-E_\theta(\mathbf{s} | g)} + e^{-E_\theta(1 - \mathbf{s} | g)} \quad (18)$$

$$F_{\text{sym}}(\mathbf{s} | g) := -\log \left(e^{-F_\theta(\mathbf{s} | g)} + e^{-F_\theta(1 - \mathbf{s} | g)} \right). \quad (19)$$

This ansatz ensures that $p_{\text{sym}}(\mathbf{s}) = p_{\text{sym}}(1 - \mathbf{s})$ by construction. While this symmetrization breaks the conditional independence of the hidden units required for standard block Gibbs sampling, we restore efficient sampling by introducing a latent symmetry variable $u \in \{0, 1\}$ into the Markov chain. The full derivation of the symmetrized free energy and the resulting *augmented Gibbs sampling* are detailed in Appendix A.1.

3.5 Training and sampling

The model parameters are trained by minimizing the KL divergence between the empirical data distribution and $p_\theta(\mathbf{s} | g)$, following the RBM training procedure reviewed in Sec. 2. Parameter updates are performed using the stochastic gradient learning rule given in Eq. (11), where the model expectation was approximated using CD- k .

For each minibatch sample (\mathbf{s}, g) , the positive phase is evaluated at the data configuration \mathbf{s} , while the negative phase is obtained from k steps of augmented Gibbs sampling scheme described in Appendix A.1 conditioned on the same value of g . To improve exploration of configuration space, a small fraction of Gibbs chains is initialized from random configurations rather than from data samples.

All RBM and hypernetwork parameters are optimized jointly using the ADAM [40] optimizer with an inverse-sigmoid learning-rate schedule.

4 EVALUATION

We assess the quality of the learned conditional wavefunction $\Psi_\theta(\mathbf{s} | g)$ using two complementary criteria. First, we evaluate local physical observables that probe operator-level properties of the state. Second, we consider global state properties such as fidelity, second-order Rényi entropies, and fidelity susceptibility, which are sensitive to the full wavefunction structure. Together, these tests probe both the local physical features and the global accuracy of the reconstructed state. All quantities are benchmarked against ED. We focus on system sizes small enough to retain numerically exact reference results, namely 1×16 chain and $L \times L$ lattices with $L \in \{3, 4\}$.

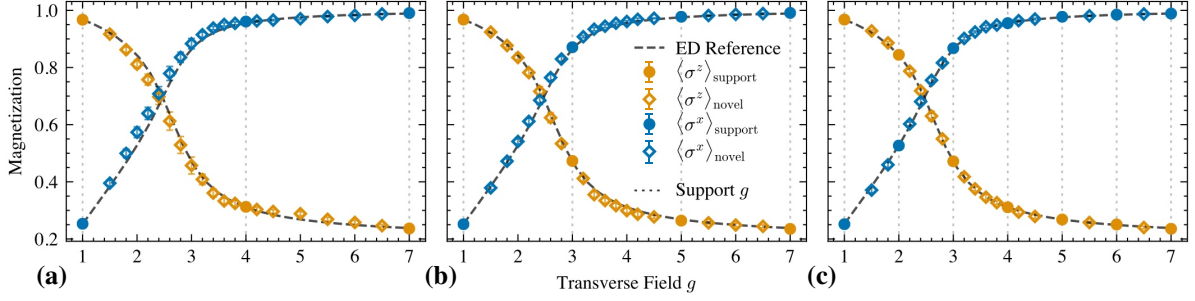


Figure 2: **Magnetization reconstruction and interpolation in g .** TFIM on the 4×4 lattice: longitudinal magnetization $\langle \sigma^z(g) \rangle$ (orange) and transverse magnetization $\langle \sigma^x(g) \rangle$ (blue) as a function of the transverse field g . Gray dashed lines show the exact-diagonalization (ED) reference. Markers show estimates from the learned conditional RBM state: filled circles are *support* fields used for training, open diamonds are *novel* fields used only for evaluation. Vertical dotted lines indicate the support locations. Panels (a)-(c) correspond to increasingly dense support sets, illustrating that adding support points improves the accuracy of interpolation on novel g values.

4.1 Benchmark I: Local observable estimation from the learned state

Given a trained model $p_\theta(\mathbf{s} | g)$, expectation values at fixed g are estimated by Monte Carlo sampling $\mathbf{s}^{(k)} \sim p_\theta(\cdot | g)$. The wavefunction representation $\Psi_\theta(\mathbf{s} | g) \propto \exp[-F_\theta(\mathbf{s} | g)/2]$ then enables local-estimator expressions based on amplitude ratios.

4.1.1 Local estimator for general observables

For a general operator \hat{O} with matrix elements $O_{\mathbf{s}'\mathbf{s}}$ $\langle \mathbf{s}' | \hat{O} | \mathbf{s} \rangle$, the expectation value can be written as

$$\langle \hat{O} \rangle_g = \sum_{\mathbf{s}, \mathbf{s}'} \Psi_\theta(\mathbf{s} | g) O_{\mathbf{s}'\mathbf{s}} \Psi_\theta(\mathbf{s}' | g), \quad (20)$$

We rewrite this as an expectation over $p_\theta(\mathbf{s} | g) = \Psi_\theta^2(\mathbf{s} | g)$,

$$\langle \hat{O} \rangle_g = \sum_{\mathbf{s}} p_\theta(\mathbf{s} | g) O_\theta^{[L]}(\mathbf{s} | g), \quad (21)$$

where the local estimator is

$$O_\theta^{[L]}(\mathbf{s} | g) := \sum_{\mathbf{s}'} O_{\mathbf{s}'\mathbf{s}} \frac{\Psi_\theta(\mathbf{s}' | g)}{\Psi_\theta(\mathbf{s} | g)}. \quad (22)$$

Using $\Psi_\theta \propto e^{-F_\theta/2}$, the amplitude ratio reduces to

$$\frac{\Psi_\theta(\mathbf{s}' | g)}{\Psi_\theta(\mathbf{s} | g)} = \exp\left[-\frac{1}{2}(F_\theta(\mathbf{s}' | g) - F_\theta(\mathbf{s} | g))\right], \quad (23)$$

so the partition function Z_θ cancels in the ratio and the local estimator is tractable provided that \hat{O} is sparse in the computational basis, i.e. for each \mathbf{s} only a small number of configurations \mathbf{s}' yield nonzero $O_{\mathbf{s}'\mathbf{s}}$. This condition is satisfied by local and few-body observables. For dense operators the evaluation of $O_\theta^{[L]}$ becomes exponentially costly. This reformulation can be viewed as an instance of importance sampling,

where configurations \mathbf{s} are sampled from $p_\theta(\mathbf{s} | g) = |\Psi_\theta(\mathbf{s} | g)|^2$ and the local estimator $O_\theta^{[L]}(\mathbf{s} | g)$ plays the role of the corresponding importance-weighted integrand.

Diagonal observables are recovered as a special case. Since only $\mathbf{s}' = \mathbf{s}$ contributes, the amplitude ratio simplifies to unity and the local estimator reduces to $O_\theta^{[L]}(\mathbf{s} | g) = O(\mathbf{s})$. The expectation value then takes the simple form

$$\langle \hat{O} \rangle_g = \sum_{\mathbf{s}} p_\theta(\mathbf{s} | g) O(\mathbf{s}) \approx \frac{1}{n_{\text{MC}}} \sum_{k=1}^{n_{\text{MC}}} O(\mathbf{s}^{(k)}). \quad (24)$$

which is estimated by Monte Carlo averaging over samples from $\mathbf{s}^{(k)} \sim p_\theta(\cdot | g)$.

4.1.2 TFIM observables

For the transverse-field Ising model, we evaluate the longitudinal magnetization

$$\langle \sigma^z(g) \rangle := \frac{1}{N} \sum_{i=1}^N \langle \sigma_i^z \rangle_g, \quad (25)$$

which reflects the change in spin alignment as the transverse field is varied. The same diagonal-estimator framework also applies to two-point correlators $\langle \sigma_i^z \sigma_j^z \rangle_g$, but we do not analyze them further and restrict attention to magnetizations.

Off-diagonal observables are accessed via the amplitude ratios as introduced in Sec. 4.1.1. In particular, the transverse magnetization can be written as

$$\langle \sigma^x(g) \rangle := \frac{1}{N} \sum_{i=1}^N \langle \sigma_i^x \rangle_g. \quad (26)$$

Equivalently, this quantity corresponds to measuring σ^z after a local Hadamard rotation on each spin, since $H\sigma^z H = \sigma^x$. In the local-estimator picture, each contribution therefore involves a single spin-flipped configuration relative to \mathbf{s} .

We report both $\langle \sigma^z(g) \rangle$ and $\langle \sigma^x(g) \rangle$ to assess whether the reconstructed state reproduces the expected behavior across the phase diagram, see Fig. 2.

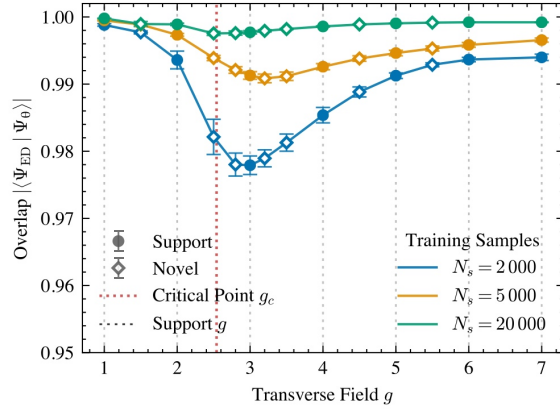


Figure 3: **Exact overlap and sample efficiency.** Exact overlap $|\langle \Psi_{\text{ED}}(g) | \Psi_{\theta}(g) \rangle|$ between the ED ground state and the reconstructed RBM state as a function of the transverse field g (here for the 4×4 TFIM). Colors denote the number of training samples per support point, $N_s \in \{2000, 5000, 20000\}$. Filled circles indicate *support* field strengths used for training, while open diamonds indicate *novel* field strengths used only for evaluation. Gray vertical dotted lines mark the support locations, and the red dotted line marks the finite-size critical field g_c . The overlap remains close to unity throughout the sweep, with the largest deviations concentrated near the crossover region and a systematic improvement as N_s increases.

4.2 Benchmark II: Global state-level comparison with exact diagonalization

For this comparison, we deliberately focus on small lattice sizes so that direct, numerically exact benchmarks against the ground state $|\Psi_{\text{ED}}(g)\rangle$ obtained by ED are possible. This provides a gold standard for state-level comparisons that does not rely on variational or approximate reference states.

4.2.1 Overlap and fidelity

We quantify agreement between learned quantum state representation and the underlying true ground state via the fidelity

$$\mathcal{F}_{\theta}(g) = |\langle \Psi_{\text{ED}}(g) | \Psi_{\theta}(g) \rangle|^2. \quad (27)$$

Since both states can be chosen real-valued and non-negative in the computational basis, the overlap re-

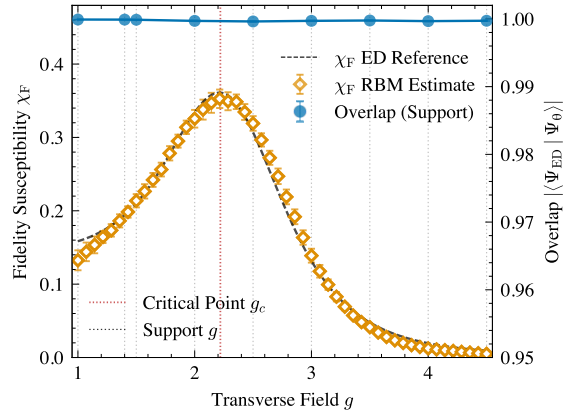


Figure 4: **Fidelity susceptibility and exact overlap.** Fidelity susceptibility $\chi_F(g)$ of the 3×3 TFIM as a function of the transverse field g . Orange diamonds show the RBM estimate obtained from variance of the free energy gradients (see Sec. 4.2.2), while the gray dashed curve is the ED reference. The blue curve (right axis) reports the ED-RBM overlap on the training support points, demonstrating near-unity state fidelity across all field strengths. Vertical gray dotted lines indicate the support field strengths, and the red dotted line marks the finite-size critical field g_c . The reconstructed $\chi_F(g)$ reproduces the ED peak in the crossover region.

duces to an explicit sum,

$$\langle \Psi_{\text{ED}}(g) | \Psi_{\theta}(g) \rangle = \sum_{\mathbf{s}} \Psi_{\text{ED}}(\mathbf{s} | g) \frac{\exp[-\frac{1}{2} F_{\theta}(\mathbf{s} | g)]}{\sqrt{Z_{\theta}(g)}}, \quad (28)$$

with $Z_{\theta}(g) = \sum_{\mathbf{s}} \exp[-F_{\theta}(\mathbf{s} | g)]$. For the system sizes considered here, $Z_{\theta}(g)$ is evaluated exactly, yielding exact fidelities (up to floating point accuracy).

For larger systems, the overlap can instead be estimated by Monte Carlo sampling. Rewriting the sum as an expectation value with respect to $p_{\theta}(\mathbf{s} | g)$ yields

$$\begin{aligned} \langle \Psi_{\text{ED}}(g) | \Psi_{\theta}(g) \rangle &= \sum_{\mathbf{s}} p_{\theta}(\mathbf{s} | g) \frac{\Psi_{\text{ED}}(\mathbf{s} | g)}{\Psi_{\theta}(\mathbf{s} | g)} \\ &= \mathbb{E}_{p_{\theta}(\mathbf{s} | g)} \left[\frac{\Psi_{\text{ED}}(\mathbf{s} | g)}{\Psi_{\theta}(\mathbf{s} | g)} \right], \end{aligned} \quad (29)$$

where the ratio involves the normalized amplitudes $\Psi_{\theta}(\mathbf{s} | g)$. For large systems, obtaining this normalization requires estimating the partition function $Z_{\theta}(g)$, which can be approximated using annealed importance sampling [41].

In practice, this estimator can suffer from large variance especially for low overlap NQS, since it involves an approximate evaluation of $Z_{\theta}(g)$. This makes Monte Carlo (MC) overlap estimation challenging for large systems. NQS representations with tractable or directly normalized amplitudes, such as autoregressive or recurrent architectures [42], may alleviate this issue and provide more stable overlap es-

timators, but exploring such approaches is left for future work.

4.2.2 Fidelity susceptibility

To probe the parametric response of the learned family of states, we compute the fidelity susceptibility, defined as the second derivative of the logarithmic fidelity with respect to a small parameter shift,

$$\chi_F(g) := -\left. \frac{\partial^2}{\partial \delta^2} \log \mathcal{F}_\theta(g, g + \delta) \right|_{\delta=0}. \quad (30)$$

Expanding the perturbed state $|\Psi_\theta(g + \delta)\rangle$ to second order in δ and evaluating the normalized overlap, one finds that all terms involving second derivatives cancel. Following standard derivations [32, 43], this yields the equivalent expression

$$\chi_F(g) = \frac{\langle \partial_g \Psi_\theta(g) | \partial_g \Psi_\theta(g) \rangle}{\langle \Psi_\theta(g) | \Psi_\theta(g) \rangle} - \frac{|\langle \Psi_\theta(g) | \partial_g \Psi_\theta(g) \rangle|^2}{\langle \Psi_\theta(g) | \Psi_\theta(g) \rangle^2}. \quad (31)$$

In practice, rather than resorting to numerical finite differences, we exploit the differentiability of the HyperRBM ansatz. As we derive in Appendix A.3, Eq. (31) can be rewritten as the variance of the gradients of the free energy:

$$\chi_F(g) = \frac{1}{4} \text{Var}_{\mathbf{s} \sim p_\theta(\cdot | g)} \left[\frac{\partial F_\theta(\mathbf{s} | g)}{\partial g} \right]. \quad (32)$$

This formulation allows us to evaluate $\chi_F(g)$ efficiently using automatic differentiation. We sample a batch of configurations from the model at a fixed g , compute the gradients $\partial_g F_\theta$ for each sample via backpropagation and calculate the sample variance. This directly assesses the coherence of the learned parametric family and enables the identification of the quantum critical point without prior knowledge of its location.

4.2.3 Rényi entropy via the replica trick

To quantify the non-local correlations captured by the reconstructed state $|\Psi_\theta(g)\rangle$, we examine the second Rényi entropy of a spatial subsystem A ,

$$S_2(A) := -\log \text{Tr}(\rho_A^2), \quad (33)$$

$$\rho_A := \text{Tr}_{A^\perp} (|\Psi_\theta(g)\rangle \langle \Psi_\theta(g)|), \quad (34)$$

which can be estimated via the *replica trick*. We briefly recap the derivation below for completeness following Refs. [44, 45].

Two-copy observable and the Swap operator. The core insight of the replica trick is that non-linear functionals of a state ρ (such as purity, $\text{Tr}(\rho^2)$) can

be expressed as linear expectation values over a tensor product of identical copies, $\rho \otimes \rho$. Related two-copy constructions also appear in quantum learning and shadow tomography, where joint measurements on $\rho^{\otimes 2}$ enable efficient estimation of Pauli observables [46, 47, 48, 49, 50, 51]. While those protocols typically employ Bell-basis measurements, the same two-copy principle underlies the swap-based purity estimator used here.

In our context, we employ the spatial Swap operator, Swap_A , which acts on the computational basis of the two replicas $\mathbf{s}^{(1)}$ and $\mathbf{s}^{(2)}$ by exchanging their configurations within subsystem A :

$$\text{Swap}_A |\mathbf{s}_A^{(1)}, \mathbf{s}_{A^\perp}^{(1)}\rangle \otimes |\mathbf{s}_A^{(2)}, \mathbf{s}_{A^\perp}^{(2)}\rangle = |\mathbf{s}_A^{(2)}, \mathbf{s}_{A^\perp}^{(1)}\rangle \otimes |\mathbf{s}_A^{(1)}, \mathbf{s}_{A^\perp}^{(2)}\rangle. \quad (35)$$

Using the identity $\text{Tr}(\rho_A^2) = \text{Tr}((\rho \otimes \rho) \text{Swap}_A)$, the purity becomes an expectation value over the joint state of the two replicas:

$$\text{Tr}(\rho_A^2) = \langle \Psi_\theta(g) | \otimes \langle \Psi_\theta(g) | \text{Swap}_A |\Psi_\theta(g)\rangle \otimes |\Psi_\theta(g)\rangle. \quad (36)$$

RBM Estimator and Free Energies. A significant advantage of combining the replica trick with Energy-Based Models like RBMs is the cancellation of normalization constants. For a fixed conditioning input g , the RBM wavefunction $\Psi_\theta(\mathbf{s} | g)$ is defined as in Eq. (15), and all quantities below are implicitly conditioned on g . When we expand the purity expectation value in the computational basis, the intractable partition functions in the numerator and denominator cancel perfectly. We are left with an estimator relying solely on the free energies F_θ :

$$\text{Tr}(\rho_A^2) = \sum_{\mathbf{s}^{(1)}, \mathbf{s}^{(2)}} p_\theta(\mathbf{s}^{(1)}) p_\theta(\mathbf{s}^{(2)}) R_A(\mathbf{s}^{(1)}, \mathbf{s}^{(2)}), \quad (37)$$

where samples are drawn from the joint distribution $p_\theta(\mathbf{s}^{(1)}) p_\theta(\mathbf{s}^{(2)})$ and the *swap ratio* R_A is given by:

$$\begin{aligned} R_A(\mathbf{s}^{(1)}, \mathbf{s}^{(2)}) &= \frac{\Psi_\theta(\mathbf{s}_A^{(2)}, \mathbf{s}_{A^\perp}^{(1)}) \Psi_\theta(\mathbf{s}_A^{(1)}, \mathbf{s}_{A^\perp}^{(2)})}{\Psi_\theta(\mathbf{s}^{(1)}) \Psi_\theta(\mathbf{s}^{(2)})} \\ &= \exp \left[-\frac{1}{2} \left(\Delta F_{\text{swap}}(\mathbf{s}^{(1)}, \mathbf{s}^{(2)}) \right) \right], \end{aligned} \quad (38)$$

with the free energy difference

$$\Delta F_{\text{swap}} = F_\theta(\mathbf{s}_A^{(2)}, \mathbf{s}_{A^\perp}^{(1)}) + F_\theta(\mathbf{s}_A^{(1)}, \mathbf{s}_{A^\perp}^{(2)}) - F_\theta(\mathbf{s}^{(1)}) - F_\theta(\mathbf{s}^{(2)}). \quad (39)$$

Thus $\text{Tr}(\rho_A^2) = \langle R_A \rangle$ with $\mathbf{s}^{(1)}, \mathbf{s}^{(2)} \sim p_\theta$ independently, which allows us to estimate $S_2(A) = -\log \langle R_A \rangle$

using standard Monte Carlo sampling without ever computing the partition function. In practice, this naive estimator can exhibit large variance for increasing subsystem size. One can alleviate this by following the improved *ratio trick* as described in Refs. [44, 45] (see also the Supplementary Material of Ref. [21]).

5 EXPERIMENTAL SETUP

We evaluate the HyperRBM ansatz on the TFIM geometries defined in Sec. 3.1, specifically a 1×16 chain and $L \times L$ square lattices with $L \in \{3, 4\}$. We start with baseline magnetization benchmarks, then vary the number of training samples per support point to study sample efficiency, and finally use the best-performing setup for the subsequent experiments. Unless stated otherwise, experiments are repeated over 10 independent random seeds, and we report the median with one standard deviation.

5.1 Training data and supports

At each support point g , we generated a pool of 20000 projective measurements in the computational basis, sufficient to cover all experiments.

The support points were chosen to span the relevant phase transitions for each geometry:

- **1D Chain:** We chose support field strengths spanning $g \in [0.5, 1.5]$ to cover the critical point at $g_c \approx 1.0$.
- **2D Lattices:** We explored a broader range $g \in [1.0, 7.0]$, covering the ferromagnetic and paramagnetic phases as well as the critical region.

For reference, ED studies on finite 2D lattices with periodic boundary conditions report finite-size critical fields g_c [52], defined as the locations where the fidelity susceptibility peaks. For the 3×3 and 4×4 cases, we use $g_c \approx 2.22$ and $g_c \approx 2.54$, respectively.

For overlap evaluation, we stored the exact ground states $|\Psi_{\text{ED}}(g)\rangle$ at all support points and at additional g values used to test interpolation.

5.2 Model architectures and protocols

We use three closely related training setups, corresponding to the different benchmarks considered below. All hyperparameters are summarized in Appendix A.4. Across all benchmarks, we use a HyperRBM with the symmetrized free-energy ansatz (Sec. 3) to enforce the global \mathbb{Z}_2 symmetry.

Magnetization interpolation. For the magnetization results in Sec. 6.1, we train models on the 4×4 lattice over $g \in [1, 7]$. The boundary points $g = 1$ and $g = 7$ are always included, while the number of intermediate support points is progressively increased.

Sample efficiency. We study sample efficiency using $N_s \in \{2000, 5000, 20000\}$ samples per support point. The resulting overlap-vs- g curves and their dependence on N_s are reported in Fig. 3 and discussed in Sec. 6.2.1.

Fidelity susceptibility. Training uses uniformly spaced support points for the 3×3 and 4×4 lattices, plus one extra support point at the lower end of the range. We estimate $\chi_F(g)$ from reconstructed states using the free-energy-gradient variance estimator described in Sec. 4.2.2. For each field value g , we draw 10^5 Monte Carlo samples for estimation. Results are shown in Fig. 4 and Fig. 1(c). For the 3×3 case, the former also shows the ED–RBM overlap on a secondary axis.

Second Rényi entropy. For the 1×16 chain, we evaluate $S_2(\ell, g)$ on a dense grid with $\Delta g = 0.05$. For each field strength, we perform extensive sampling using up to 3×10^5 model samples and 20 Gibbs steps. This allows us to get smooth results despite relying on the naive swap estimator (Sec. 4.2.3). Results are reported in Fig. 5 (Sec. 6.2.3).

6 RESULTS

6.1 Benchmark I: Magnetizations and interpolation in g

We first benchmark the learned conditional state using local observables, focusing on the transverse and longitudinal magnetizations $\langle \sigma^x(g) \rangle$ and $\langle \sigma^z(g) \rangle$.

To assess interpolation in the control parameter g , we evaluate the trained model on a fixed grid of 21 field values spanning $g \in [1, 7]$, including both training support points and unseen values. This evaluation is repeated while progressively increasing the number of support points, as shown in Fig. 2 from left to right.

Across all support densities, the reconstructed magnetizations reproduce the expected physical behavior: the longitudinal magnetization decreases monotonically with increasing g , while $\langle \sigma^x(g) \rangle$ increases and approaches unity at large fields. The most pronounced variation occurs in the finite-size crossover region, where both observables change

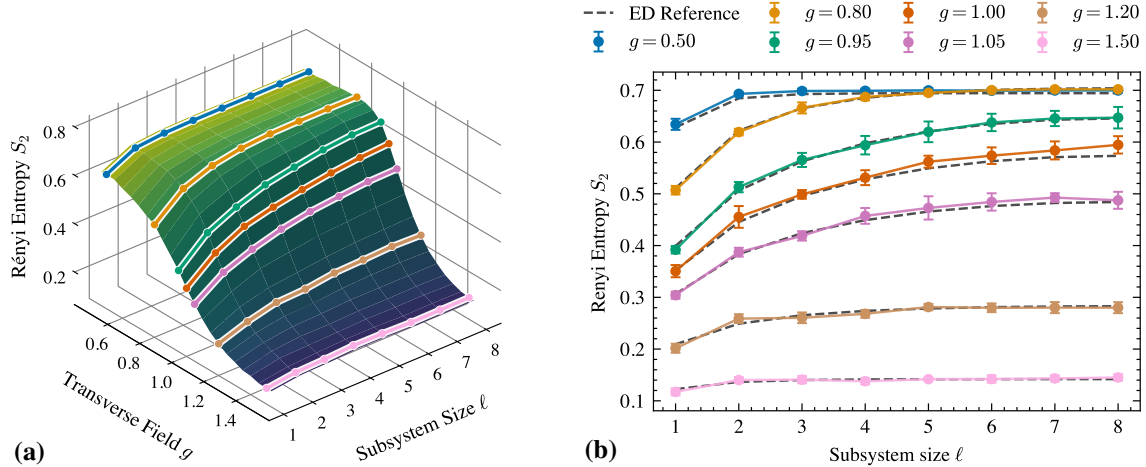


Figure 5: Second Rényi entropy across the TFIM transition. TFIM on the 1×16 chain: second Rényi entropy $S_2(\ell, g)$ of a contiguous subsystem of size ℓ (Sec. 4.2.3). **(a)** RBM estimate evaluated on a dense grid ($\Delta g = 0.05$) on control parameter g , revealing a steep gradient around $g \approx 1$ that is captured smoothly as a function of g . Colored overlay curves indicate the training support fields strengths. **(b)** Overlaid $S_2(\ell)$ slices at different support fields g : solid colored curves (markers) are RBM estimates and black dashed curves show the exact-diagonalization (ED) reference. The RBM reproduces both the transition-associated drop and the expected entropy scale, saturating near $S_2 \approx \ln 2$ for this finite system.

rapidly in opposite directions. Deep in the paramagnetic regime, $\langle \sigma^x(g) \rangle$ saturates near 1, while the longitudinal magnetization approaches a small finite-size plateau.

Notably, even with only three support points, the reconstructed magnetizations already show good agreement with the exact curves (Fig. 2(a)). Increasing the support density primarily refines the reconstruction in the finite-size crossover region.

6.2 Benchmark II: Global state-level properties

We next assess the learned wavefunction at the state level using global properties, including overlap, fidelity susceptibility, and the second-order Rényi entropy.

6.2.1 Exact overlap and sample efficiency

Figure 3 shows the overlap $|\langle \Psi_{\text{ED}}(g) | \Psi_{\theta}(g) \rangle|$ on the 4×4 lattice for different numbers of training samples per support point. The overlap remains close to one across the full range of g , with the largest deviations occurring in the crossover region near the finite-size critical field g_c . Even for $N_s = 2000$ samples per support point, the fidelity exceeds 99% outside the crossover region and remains above 98% at its minimum. Increasing the dataset size systematically reduces this dip and improves interpolation at novel g

values, while the overlap rapidly saturates outside the crossover region for all training regimes.

Based on this behavior, we use $N_s = 20000$ samples per support point for the fidelity-susceptibility calculations, where higher precision is desired.

6.2.2 Fidelity susceptibility from reconstructed states

Figure 4 reports the fidelity susceptibility $\chi_F(g)$ on the 3×3 lattice, computed via the variance of the free-energy gradients. The RBM estimate follows the ED reference and reproduces the peak in the crossover region near g_c , suggesting that the conditional model captures the parametric response. At the same time, the ED–RBM overlap on the support points remains near unity (blue curve), confirming that the susceptibility agreement is consistent with high global state fidelity.

Figure 1(c) demonstrates similar accuracy on the 4×4 lattice, where the model correctly identifies the susceptibility peak around the critical field $g_c \approx 2.54$.

6.2.3 Second Rényi entropy: non-local correlations and interpolation in g

Figure 5 benchmarks the learned conditional family using the second Rényi entropy $S_2(\ell, g)$ on the 1×16 chain. Evaluating the RBM on a dense grid of fields yields the surface shown in Fig. 5a. The smoothness of the surface demonstrates that the model success-

fully interpolates the wavefunction continuously in g . Consequently, the conditional state faithfully resolves the steep gradient in entanglement entropy around the critical point $g \approx 1$ without requiring point-wise re-training.

Figure 5b details the corresponding $S_2(\ell)$ slices at different support fields g overlaid in a single panel. The RBM estimates closely follow the ED reference across all cuts and reproduce the expected entropy scale, saturating near $S_2 \approx \ln 2$ in the ferromagnetic phase. We observe the largest deviations at the largest subsystems, consistent with the increased variance of swap-based estimators for large ℓ (Sec. 4.2.3).

7 CONCLUSION & OUTLOOK

We introduced a parametric quantum state tomography (pQST) framework based on a hypernetwork-conditioned RBM (HyperRBM) for ground states of the one- and two-dimensional transverse-field Ising model. The transverse field strength g acts as a continuous control parameter and modulates the RBM biases via FiLM. On a 1×16 chain and $L \times L$ for $L \in \{3, 4\}$ lattices, we showed that a single conditional model for each lattice size can represent a continuous family of ground states across the phase diagram. The learned states reproduce key physical signatures, including transverse and longitudinal magnetizations, already with modest training data. With sufficient samples, the HyperRBM achieves high overlap with the exact ground states (exceeding 99%) across both phases and remains accurate in the critical region. In addition, we accurately estimate second-order Rényi entropies for the 1D chain using extensive sampling, indicating that the approach captures non-local correlations and entanglement structure. Finally, treating the reconstructed states as a coherent parametric family, we extract the fidelity susceptibility for 2D lattices and identify the quantum critical point without prior knowledge of its location or an explicit order parameter. All results were obtained with modest computational resources, relying exclusively on CPU-based training and sampling (details in Appendix A.2).

In this work, system sizes were limited by the use of exact diagonalization for ground-truth fidelities and susceptibility benchmarks. A natural next step is to combine HyperRBMs with scalable data generation techniques, such as quantum Monte Carlo or tensor-network methods, to extend parametric tomography to larger lattices.

Beyond the TFIM, an important next step is to extend parametric tomography to non-stoquastic

Hamiltonians. This can be achieved by combining the present conditioning scheme with the general complex-valued RBM ansatz introduced in Ref. [21], where separate networks parameterize amplitudes and phases. In this setting, the hypernetwork would condition both amplitude and phase parameters, enabling parametric learning of genuinely complex-valued quantum states. Preliminary experiments indicate that the approach extends beyond stoquastic models when combined with complex-valued RBM ansatzes, although a systematic study is left for future work.

Besides improving sample and training efficiency, this structured conditioning also supports interpretability analyses. Because physical control parameters act through a low-dimensional modulation pathway, one can inspect how changes in the Hamiltonian translate into structured updates of model parameters and how these responses evolve across phases or near critical points. More broadly, it remains an open question whether hypernetwork-equipped NQS can provide a flexible framework for learning physically meaningful manifolds of quantum states, including thermal or parameter-dependent dynamical states.

CODE AND DATA AVAILABILITY

The code used to generate the results and the datasets analyzed in this study will be made available at <https://github.com/simontonner/hyperrbm-parametric-qst>. [53]

ACKNOWLEDGEMENTS

AI tools such as ChatGPT (GPT-5 series) and Gemini (Gemini 3 Pro) were used to refine phrasing in parts of the manuscript and to assist with figure styling. All results and final wording were reviewed and validated by the authors.

The team at JKU Linz acknowledges funding from the European Research Council (ERC) via the Starting grant q-shadows (101117138) and from the Austrian Science Fund (FWF) via the SFB BeyondC (10.55776/FG7).

References

- [1] Daniel F. V. James et al. “Measurement of qubits”. In: *Physical Review A* 64.5 (2001). Publisher: American Physical Society,

p. 052312. DOI: 10.1103/PhysRevA.64.052312.

[2] *Quantum State Estimation*. Vol. 649. Springer, 2004. DOI: 10.1007/b98673.

[3] K Banaszek, M Cramer, and D Gross. “Focus on quantum tomography”. In: *New Journal of Physics* 15.12 (2013). Publisher: IOP Publishing, p. 125020. DOI: 10.1088/1367-2630/15/12/125020.

[4] G. Tóth et al. “Permutationally Invariant Quantum Tomography”. In: *Physical Review Letters* 105.25 (2010). Publisher: American Physical Society, p. 250403. DOI: 10.1103/PhysRevLett.105.250403.

[5] Christian Schwemmer et al. “Experimental Comparison of Efficient Tomography Schemes for a Six-Qubit State”. In: *Physical Review Letters* 113.4 (2014). Publisher: American Physical Society, p. 040503. DOI: 10.1103/PhysRevLett.113.040503.

[6] Ryan O’Donnell and John Wright. “Efficient quantum tomography”. In: *Proceedings of the Forty-Eighth Annual ACM Symposium on Theory of Computing*. 2016, pp. 899–912. DOI: 10.1145/2897518.2897544.

[7] Jeongwan Haah et al. “Sample-optimal tomography of quantum states”. In: *Proceedings of the Forty-Eighth Annual ACM Symposium on Theory of Computing*. 2016, pp. 913–925. DOI: 10.1145/2897518.2897585.

[8] Richard Kueng, Holger Rauhut, and Ulrich Terstiege. “Low rank matrix recovery from rank one measurements”. In: *Applied and Computational Harmonic Analysis* 42.1 (2017), pp. 88–116. DOI: doi.org/10.1016/j.acha.2015.07.007.

[9] Daniel Stilck França, Fernando G. S. L. Brandão, and Richard Kueng. “Fast and Robust Quantum State Tomography from Few Basis Measurements”. In: *16th Conference on the Theory of Quantum Computation, Communication and Cryptography, TQC 2021, July 5-8, 2021, Virtual Conference*. Vol. 197. 2021, 7:1–7:13. DOI: 10.4230/LIPICS.TQC.2021.7.

[10] Angelos Pelecanos et al. *Mixed state tomography reduces to pure state tomography*. arXiv:2511.15806 [quant-ph]. 2025. DOI: 10.48550/arXiv.2511.15806.

[11] Scott Aaronson. “Shadow tomography of quantum states”. In: *Proceedings of the 50th Annual ACM SIGACT Symposium on Theory of Computing*. 2018, pp. 325–338. DOI: 10.1145/3188745.3188802.

[12] Hsin-Yuan Huang, Richard Kueng, and John Preskill. “Predicting many properties of a quantum system from very few measurements”. In: *Nature Physics* 16.10 (2020). Publisher: Nature Publishing Group, pp. 1050–1057. DOI: 10.1038/s41567-020-0932-7.

[13] Andreas Elben et al. “The randomized measurement toolbox”. In: *Nature Reviews Physics* 5.1 (2023). Publisher: Nature Publishing Group, pp. 9–24. DOI: 10.1038/s42254-022-00535-2.

[14] Hsin-Yuan Huang et al. “Provably efficient machine learning for quantum many-body problems”. In: *Science* 377.6613 (2022). Publisher: American Association for the Advancement of Science, eabk3333. DOI: 10.1126/science.eabk3333.

[15] Laura Lewis et al. “Improved machine learning algorithm for predicting ground state properties”. In: *Nature Communications* 15.1 (2024). Publisher: Nature Publishing Group, p. 895. DOI: 10.1038/s41467-024-45014-7.

[16] Marc Wanner et al. “Predicting ground state properties: constant sample complexity and deep learning algorithms”. In: *Proceedings of the 38th International Conference on Neural Information Processing Systems*. 2024. arXiv: 2405.18489 [quant-ph].

[17] Marcus Cramer et al. “Efficient quantum state tomography”. In: *Nature Communications* 1.1 (2010). Publisher: Nature Publishing Group, p. 149. DOI: 10.1038/ncomms1147.

[18] T. Baumgratz et al. “Scalable Reconstruction of Density Matrices”. In: *Physical Review Letters* 111.2 (2013). Publisher: American Physical Society, p. 020401. DOI: 10.1103/PhysRevLett.111.020401.

[19] David Gross et al. “Quantum State Tomography via Compressed Sensing”. In: *Physical Review Letters* 105.15 (2010). Publisher: American Physical Society, p. 150401. DOI: 10.1103/PhysRevLett.105.150401.

[20] Giuseppe Carleo and Matthias Troyer. “Solving the quantum many-body problem with artificial neural networks”. In: *Science* 355.6325 (2017). Publisher: American Association for the Advancement of Science, pp. 602–606. DOI: 10.1126/science.aag2302.

[21] Giacomo Torlai et al. “Neural-network quantum state tomography”. In: *Nature Physics* 14.5 (2018), pp. 447–450. DOI: 10.1038/s41567-018-0048-5.

[22] Yusuke Nomura et al. “Restricted Boltzmann machine learning for solving strongly correlated quantum systems”. In: *Physical Review B* 96.20 (2017). Publisher: American Physical Society, p. 205152. DOI: 10.1103/PhysRevB.96.205152.

[23] Franz J. Schreiber, Jens Eisert, and Johannes Jakob Meyer. “Tomography of Parametrized Quantum States”. In: *PRX Quantum* 6.2 (2025), p. 020346. DOI: 10.1103/PRXQuantum.6.020346.

[24] Shahnawaz Ahmed et al. “Quantum State Tomography with Conditional Generative Adversarial Networks”. In: *Physical Review Letters* 127.14 (2021), p. 140502. DOI: 10.1103/PhysRevLett.127.140502.

[25] David Ha, Andrew M. Dai, and Quoc V. Le. “HyperNetworks”. In: *Proceedings of the International Conference on Learning Representations (ICLR)*. 2017. arXiv: 1609.09106 [cs.LG].

[26] Johannes von Oswald et al. “Continual learning with hypernetworks”. In: *International Conference on Learning Representations (ICLR)*. 2020. arXiv: 1906.00695 [cs.LG].

[27] Emma Svensson et al. “HyperPCM: Robust Task-Conditioned Modeling of Drug–Target Interactions”. In: *Journal of Chemical Information and Modeling* 64.7 (2024), pp. 2539–2553. DOI: 10.1021/acs.jcim.3c01417.

[28] Tsendsuren Munkhdalai and Hong Yu. “Meta networks”. In: *Proceedings of the 34th International Conference on Machine Learning - Volume 70*. 2017, pp. 2554–2563. arXiv: 1703.00837.

[29] Neale Ratzlaff and Li Fuxin. “HyperGAN: A Generative Model for Diverse, Performant Neural Networks”. In: *Proceedings of the 36th International Conference on Machine Learning*. ISSN: 2640-3498. 2019, pp. 5361–5369. arXiv: 1901.11058 [cs.LG].

[30] Ethan Perez et al. “FiLM: Visual Reasoning with a General Conditioning Layer”. In: *Proceedings of the 32nd AAAI Conference on Artificial Intelligence (AAAI-18)*. 2018, pp. 3942–3951. DOI: 10.1609/aaai.v32i1.11671.

[31] Paolo Zanardi and Nikola Paunković. “Ground state overlap and quantum phase transitions”. In: *Physical Review E* 74.3 (2006). Publisher: American Physical Society, p. 031123. DOI: 10.1103/PhysRevE.74.031123.

[32] Paolo Zanardi, Paolo Giorda, and Marco Cozzini. “Information-Theoretic Differential Geometry of Quantum Phase Transitions”. In: *Physical Review Letters* 99.10 (2007). Publisher: American Physical Society, p. 100603. DOI: 10.1103/PhysRevLett.99.100603.

[33] Juan Carrasquilla and Roger G. Melko. “Machine learning phases of matter”. In: *Nature Physics* 13.5 (2017). Publisher: Nature Publishing Group, pp. 431–434. DOI: 10.1038/nphys4035.

[34] Evert P. L. van Nieuwenburg, Ye-Hua Liu, and Sebastian D. Huber. “Learning phase transitions by confusion”. In: *Nature Physics* 13.5 (2017). Publisher: Nature Publishing Group, pp. 435–439. DOI: 10.1038/nphys4037.

[35] Korbinian Kottmann et al. “Unsupervised Phase Discovery with Deep Anomaly Detection”. In: *Physical Review Letters* 125.17 (2020). Publisher: American Physical Society, p. 170603. DOI: 10.1103/PhysRevLett.125.170603.

[36] Sergey Bravyi et al. “The complexity of stoquastic local Hamiltonian problems”. In: *Quantum Info. Comput.* 8.5 (2008), pp. 361–385. arXiv: quant-ph/0606140 [quant-ph].

[37] Geoffrey E. Hinton. “Training Products of Experts by Minimizing Contrastive Divergence”. In: *Neural Computation* 14.8 (2002), pp. 1771–1800. DOI: 10.1162/089976602760128018.

[38] Geoffrey E. Hinton. “A Practical Guide to Training Restricted Boltzmann Machines”. In: *Neural Networks: Tricks of the Trade: Second Edition*. Springer, 2012, pp. 599–619. DOI: 10.1007/978-3-642-35289-8_32.

[39] Volodymyr Mnih, Hugo Larochelle, and Geoffrey E. Hinton. “Conditional restricted Boltzmann machines for structured output prediction”. In: *Proceedings of the Twenty-Seventh Conference on Uncertainty in Artificial Intelligence*. 2011, pp. 514–522. arXiv: 1202.3748 [cs.LG].

[40] Diederik P. Kingma and Jimmy Ba. “Adam: A Method for Stochastic Optimization”. In: *3rd International Conference on Learning Representations, ICLR 2015, San Diego, CA, USA, May 7-9, 2015, Conference Track Proceedings*. 2015. arXiv: 1412.6980 [cs.LG].

[41] Ruslan Salakhutdinov and Iain Murray. “On the quantitative analysis of deep belief networks”. In: *Proceedings of the 25th international conference on Machine learning - ICML '08*. 2008, pp. 872–879. DOI: 10.1145/1390156.1390266.

[42] Mohamed Hibat-Allah et al. “Recurrent neural network wave functions”. In: *Physical Review Research* 2.2 (2020). Publisher: American Physical Society, p. 023358. DOI: 10.1103/PhysRevResearch.2.023358.

[43] Shi-Jian Gu. “Fidelity approach to quantum phase transitions”. In: *International Journal of Modern Physics B* 24.23 (2010). arXiv:0811.3127 [quant-ph], pp. 4371–4458. DOI: 10.1142/S0217979210056335.

[44] Matthew B. Hastings et al. “Measuring Renyi Entanglement Entropy in Quantum Monte Carlo Simulations”. In: *Physical Review Letters* 104.15 (2010). Publisher: American Physical Society, p. 157201. DOI: 10.1103/PhysRevLett.104.157201.

[45] Giacomo Torlai. “Augmenting Quantum Mechanics with Artificial Intelligence”. PhD thesis. University of Waterloo, 2018.

[46] Sitan Chen, Weiyuan Gong, and Qi Ye. “Optimal Tradeoffs for Estimating Pauli Observables”. In: *2024 IEEE 65th Annual Symposium on Foundations of Computer Science (FOCS)*. ISSN: 2575-8454. 2024, pp. 1086–1105. DOI: 10.1109/FOCS61266.2024.00072.

[47] Robbie King et al. “Triply efficient shadow tomography”. In: *Proceedings of the 2025 Annual ACM-SIAM Symposium on Discrete Algorithms (SODA)*. Society for Industrial and Applied Mathematics, 2025, pp. 914–946. DOI: 10.1137/1.9781611978322.27.

[48] Hsin-Yuan Huang, Richard Kueng, and John Preskill. “Information-Theoretic Bounds on Quantum Advantage in Machine Learning”. In: *Physical Review Letters* 126.19 (2021). Publisher: American Physical Society, p. 190505. DOI: 10.1103/PhysRevLett.126.190505.

[49] Hsin-Yuan Huang et al. “Quantum advantage in learning from experiments”. In: *Science* 376.6598 (2022). Publisher: American Association for the Advancement of Science, pp. 1182–1186. DOI: 10.1126/science.abn7293.

[50] Viet T. Tran and Richard Kueng. “One, Two, Three: One Empirical Evaluation of a Two-Copy Shadow Tomography Scheme with Triple Efficiency”. In: *2025 IEEE International Conference on Quantum Computing and Engineering (QCE)*. Vol. 01. 2025, pp. 1599–1610. DOI: 10.1109/QCE65121.2025.00177.

[51] Jan Nöller et al. *An infinite hierarchy of multi-copy quantum learning tasks*. arXiv:2510.08070 [quant-ph]. 2025. DOI: 10.48550/arXiv.2510.08070.

[52] Wing-Chi Yu et al. “Fidelity susceptibility in the two-dimensional transverse-field Ising and XXZ models”. In: *Physical Review E* 80.2 (2009). Publisher: American Physical Society, p. 021108. DOI: 10.1103/PhysRevE.80.021108.

[53] Simon Tonner, Viet T. Tran, and Richard Kueng. *Code for "Parametric Quantum State Tomography with HyperRBMs"*. Online. Available: <https://github.com/simontonner/hyperrbm-parametric-qst> (to be uploaded shortly). 2025.

[54] Martin A. Tanner and Wing Hung Wong. “The Calculation of Posterior Distributions by Data Augmentation”. In: *Journal of the American Statistical Association* 82.398 (1987). Publisher: [American Statistical Association, Taylor & Francis, Ltd.], pp. 528–540. DOI: 10.2307/2289457.

A APPENDIX

A.1 Symmetrized ansatz and augmented sampling

A.1.1 Symmetrized Free Energy

In the ferromagnetic phase of the TFIM ($g < J$), the ground state is doubly degenerate. To strictly enforce the physical \mathbb{Z}_2 spin-flip symmetry, we define the model probability as a mixture of the standard RBM energy $E_\theta(\mathbf{s})$ and the energy of the flipped configuration $E_\theta(1 - \mathbf{s})$. The effective free energy $F_{\text{sym}}(\mathbf{s})$

is:

$$F_{\text{sym}}(\mathbf{s}) = -\ln \left(e^{-F_{\theta}(\mathbf{s})} + e^{-F_{\theta}(1-\mathbf{s})} \right), \quad (40)$$

where $F_{\theta}(\mathbf{s})$ is the standard RBM free energy. The term for the flipped configuration is computed efficiently using the identity $(1-\mathbf{s})^T \mathbf{W} = \Sigma_W^T - \mathbf{s}^T \mathbf{W}$, where Σ_W is the vector of column sums of \mathbf{W} .

A.1.2 Augmented Gibbs Sampling

Standard block Gibbs sampling is inapplicable because the symmetrized mixture distribution breaks the conditional independence of hidden units. We employ a data augmentation scheme [54] by introducing a binary latent variable $u \in \{0, 1\}$ ($u = 0$: normal, $u = 1$: flipped). Conditioned on u , independence is restored.

The sampling procedure is a three-step alternating Gibbs chain. We define $\text{sigmoid}(x) = (1 + e^{-x})^{-1}$.

1. Sample Hidden Units ($\mathbf{s}, u \rightarrow \mathbf{h}$). Calculate the effective input $\tilde{\mathbf{s}} = \mathbf{s}$ if $u = 0$, or $\tilde{\mathbf{s}} = 1 - \mathbf{s}$ if $u = 1$. Sample hidden units independently:

$$p(h_j = 1 | \mathbf{s}, u) = \text{sigmoid} \left(c_j(g) + \sum_i \tilde{s}_i W_{ij} \right). \quad (41)$$

2. Sample Symmetry Variable ($\mathbf{s}, \mathbf{h} \rightarrow u'$). We compare the energy of the current configuration against its flipped counterpart. Define the energy difference $\Delta E = E_{\theta}(1 - \mathbf{s}, \mathbf{h}) - E_{\theta}(\mathbf{s}, \mathbf{h})$. The probability of switching to the flipped sector is:

$$p(u' = 1 | \mathbf{s}, \mathbf{h}) = \text{sigmoid}(-\Delta E). \quad (42)$$

3. Sample Visible Units ($\mathbf{h}, u' \rightarrow \mathbf{s}'$). Generate a prototype vector $\mathbf{s}_{\text{proto}}$ using the standard RBM conditional $p(s_i = 1 | \mathbf{h}) = \text{sigmoid}(b_i(g) + \sum_j W_{ij} h_j)$. Apply the symmetry transform:

$$\mathbf{s}' = \begin{cases} \mathbf{s}_{\text{proto}} & \text{if } u' = 0 \\ 1 - \mathbf{s}_{\text{proto}} & \text{if } u' = 1. \end{cases} \quad (43)$$

A.2 Compute resources

All experiments were conducted on CPU on an Apple MacBook Pro (M1 Pro) with 16 GB RAM. Except for runs with extensive Monte Carlo sampling, neither memory nor CPU utilization approached saturation. No individual training or sampling run exceeded 30 minutes.

A.3 Derivation of fidelity susceptibility via variance

Here we derive the connection between the fidelity susceptibility and the variance of the free energy gradients used in Sec. 4.2.2.

We start from the geometric definition of the fidelity susceptibility given in Eq. (31):

$$\chi_F(g) = \frac{\langle \partial_g \Psi_{\theta} | \partial_g \Psi_{\theta} \rangle}{\langle \Psi_{\theta} | \Psi_{\theta} \rangle} - \left(\frac{\langle \Psi_{\theta} | \partial_g \Psi_{\theta} \rangle}{\langle \Psi_{\theta} | \Psi_{\theta} \rangle} \right)^2, \quad (31)$$

where we have suppressed the dependency on g for brevity and assumed real-valued wavefunctions. We express the wavefunction gradients using the log-derivative identity $\partial_g \Psi_{\theta}(\mathbf{s}) = \Psi_{\theta}(\mathbf{s}) \partial_g \ln \Psi_{\theta}(\mathbf{s})$.

The first term corresponds to the second moment. By explicitly writing out the inner product sum and grouping the normalization factor $\langle \Psi_{\theta} | \Psi_{\theta} \rangle$, we recover the model probability $p_{\theta}(\mathbf{s}) = |\Psi_{\theta}(\mathbf{s})|^2 / \langle \Psi_{\theta} | \Psi_{\theta} \rangle$:

$$\begin{aligned} \frac{\langle \partial_g \Psi_{\theta} | \partial_g \Psi_{\theta} \rangle}{\langle \Psi_{\theta} | \Psi_{\theta} \rangle} &= \frac{1}{\langle \Psi_{\theta} | \Psi_{\theta} \rangle} \sum_{\mathbf{s}} \left(\Psi_{\theta}(\mathbf{s}) \frac{\partial \ln \Psi_{\theta}(\mathbf{s})}{\partial g} \right)^2 \\ &= \sum_{\mathbf{s}} \underbrace{\frac{|\Psi_{\theta}(\mathbf{s})|^2}{\langle \Psi_{\theta} | \Psi_{\theta} \rangle}}_{p_{\theta}(\mathbf{s})} \left(\frac{\partial \ln \Psi_{\theta}(\mathbf{s})}{\partial g} \right)^2 \\ &= \mathbb{E}_{p_{\theta}} \left[(\partial_g \ln \Psi_{\theta})^2 \right]. \end{aligned} \quad (44)$$

Similarly, the second term corresponds to the squared first moment. The denominator cancels against the state amplitudes in the inner product to again yield the probability weight $p_{\theta}(\mathbf{s})$:

$$\begin{aligned} \frac{\langle \Psi_{\theta} | \partial_g \Psi_{\theta} \rangle}{\langle \Psi_{\theta} | \Psi_{\theta} \rangle} &= \frac{1}{\langle \Psi_{\theta} | \Psi_{\theta} \rangle} \sum_{\mathbf{s}} \Psi_{\theta}(\mathbf{s}) \left(\Psi_{\theta}(\mathbf{s}) \frac{\partial \ln \Psi_{\theta}(\mathbf{s})}{\partial g} \right) \\ &= \sum_{\mathbf{s}} \underbrace{\frac{|\Psi_{\theta}(\mathbf{s})|^2}{\langle \Psi_{\theta} | \Psi_{\theta} \rangle}}_{p_{\theta}(\mathbf{s})} \frac{\partial \ln \Psi_{\theta}(\mathbf{s})}{\partial g} \\ &= \mathbb{E}_{p_{\theta}} [\partial_g \ln \Psi_{\theta}]. \end{aligned} \quad (45)$$

The fidelity susceptibility is the difference between these two moments, which is exactly the variance:

$$\chi_F(g) = \mathbb{E}_{p_{\theta}} [(\dots)^2] - (\mathbb{E}_{p_{\theta}} [\dots])^2 \quad (46)$$

$$= \text{Var}_{\mathbf{s} \sim p_{\theta}} \left[\frac{\partial \ln \Psi_{\theta}(\mathbf{s})}{\partial g} \right]. \quad (47)$$

For the RBM ansatz $\Psi_{\theta}(\mathbf{s}) = e^{-F_{\theta}(\mathbf{s})/2} / \sqrt{Z_{\theta}}$, the log-derivative is:

$$\frac{\partial \ln \Psi_{\theta}}{\partial g} = -\frac{1}{2} \frac{\partial F_{\theta}(\mathbf{s})}{\partial g} - \frac{1}{2} \frac{\partial \ln Z_{\theta}}{\partial g}. \quad (48)$$

Since the partition function term $\partial_g \ln Z_\theta$ is independent of the configuration \mathbf{s} , it acts as an additive constant. Because the variance is translation invariant ($\text{Var}[X + c] = \text{Var}[X]$), this term vanishes, yielding the final expression:

$$\chi_F(g) = \frac{1}{4} \text{Var}_{\mathbf{s} \sim p_\theta} [\partial_g F_\theta(\mathbf{s})]. \quad (49)$$

Table 1: **Table A.1** — Hyperparameter settings across experimental tasks.

Parameter	Magnetization	Sample Efficiency	Fidelity Susceptibility	Rényi Entropy
System				
Geometry	2D (4×4)	2D (4×4)	2D (4×4 & 3×3)	Chain ($L = 16$)
Train. Supports	var. ($g \in [1.0, 7.0]$)	7 ($g \in [1.0, 7.0]$)	9 ($g \in [1.0, 4.5]$)	7 ($g \in [0.5, 1.5]$)
Train. Samples / Supp.	$20k$	$2k / 5k / 20k$	$20k$	$20k$
Architecture				
Hidden Units	64	64	64	64
Hypernet. Width	64	64	64	64
Training				
Epochs	50	50	50	50
Batch Size	1024	1024	1024	1024
CD- k Steps	10	10	20	20
Chain Init.	Data + 10% Noise	Data + 10% Noise	Data + 10% Noise	Data + 10% Noise
Weight Init. (STD)	0.01	0.05	0.01	0.01
LR Sigmoid Schedule	$10^{-2} \rightarrow 10^{-4}$	$10^{-2} \rightarrow 10^{-4}$	$10^{-2} \rightarrow 10^{-4}$	$10^{-2} \rightarrow 10^{-4}$
Evaluation				
Method	MC Sampling	Exact via Z_θ	MC Sampling	MC Sampling
Eval. Samples	1k	N/A	5k	20k
Eval. CD- k Steps	10	N/A	20	20

A.4 Hyperparameter configuration